Check for updates

Al filament-induced unipolar resistive switching in sputtered Al-rich AlN memristors with low operating voltage and high memory window

Ankang Xiao, [ID] [a] Luyu Zhao,[a] Ying Yang,[a] Cai Jin,[a] Xiaoqin Yang,[a] Lili Ma,[a] Feifei Tian,[b] Wei Hu, [ID] [c] Zengli Huang[a] and Hong Gu*[a]

Aluminum nitride (AlN) films were deposited on W/Ti/SiO$_2$/Si substrates using magnetron sputtering to fabricate AlN-based resistive random-access memory (RRAM) devices. By modulating the nitrogen-to-argon ratio (N$_2$/Ar) to form Al-rich (non-stoichiometric) AlN films, we achieved regulated unipolar RRAM devices with low set voltages (~1 V) and reset voltages (~0.5 V), exhibiting a significant memory window exceeding 10^5 and retention time of ~10^3 s. The underlying mechanisms of resistive switching were explored through the analysis of the electrical performance, X-ray photoelectron spectroscopy (XPS) characterization, a variable temperature test and conduction mechanism studies. These analyses confirm that the electroformation of conductive filaments within Al-rich AlN films is responsible for the observed unipolar switching behavior. The fabricated unipolar memristors with low voltage and high on/off ratio hold great potential for future high-density multi-level arrays and low-voltage RRAM devices, offering promising prospects for efficient computing.

AlN, a wide-bandgap material characterized by its high breakdown electric field, excellent thermal conductivity, significant dielectric constant, and outstanding stability is particularly suitable for advanced memory technologies.[1–3] Research on AlN memristors, initiated around 2010 with stable Cu/AlN/Pt devices, has shown promising progress.[4] Recent research focuses on optimizing the resistive switching layer and device structure, including film growth,[5] material modifications,[6,7] and interface layer introduction.[8] For example, The Hewlett-Packard Laboratories research team fabricated TiN/AlN/Pt nanowire-based memristors, and demonstrated high-speed operation with a switching time of 85 ps.[9] Among these, Unipolar memristors, which operate with single-polarity voltage for both set and reset, offer simpler circuit design and fabrication, facilitating compact, efficient memory solutions.[10,11] Integrating these into high-density crossbar arrays using one diode and one memristor connected in series (a 1D1R configuration) supports compact, high-density memory architectures (four F squared, $4F^2$) with high switching speeds.[12,13] However, obtaining unipolar memristors with both low operating voltage and high switching on/off ratio is still a challenge and needs to be further explored. Recent advances in thin-film fabrication technologies provide the possibility for high-quality film growth to realize material modification and functional integration. Among them, magnetron sputtering stands out as a simple, CMOS-compatible, readily controllable method for stoichiometry and composition,[14,15] and plays a pivotal role in high-quality AlN film growth.[16–18] At the same time, there are limited studies investigating the impact of non-stoichiometric composition on the unipolar resistive switching characteristics of AlN-based memristors, particularly those aimed at achieving low voltage and high switching on/off ratio *via* magnetron sputtering techniques.

This study investigates the preparation of Al-rich AlN-based RRAM devices using a straightforward and adaptable magnetron sputtering technique to control unipolar resistive switching characteristics. By modulating the N$_2$/Ar ratio to control stoichiometry, we successfully fabricated unipolar Al/AlN/W devices featuring low set voltages (~1 V) and reset voltages (~0.5 V) and high on/off current ratios exceeding 10^5. Preliminary investigations suggest that the switching behavior can be attributed to the electroformation of conductive filaments within the Al-rich AlN layer. The development of such tunable, low-voltage and wide-resistance-window AlN-based memristors holds significant promise for future high-density multi-level arrays and low-voltage RRAM devices.

A 100 nm-thick tungsten (W) film was deposited *via* electron-beam evaporation onto Ti/SiO$_2$/Si substrates to serve as the bottom electrode. Subsequently, AlN films were deposited on

Information Materials Research Department, Suzhou Laboratory, Suzhou 215123, China. E-mail: guh@szlab.ac.cn

Testing and Analysis Platform, Suzhou Institute of Nano-technology and Nano-Bionics, Suzhou 215123, China

Key Laboratory of Optoelectronic Technology and System of Ministry of Education, College of Optoelectronic Engineering, Chongqing University, Chongqing 400044, China

the W electrodes by magnetron sputtering at a substrate temperature of 25 °C, employing a sputtering power of 450 W, a working pressure of 5 mTorr, and a fixed N_2/Ar gas flow ratio of 3 : 1. To obtain AlN films of varying thicknesses, the deposition duration was systematically controlled at 2.5, 5, 7.5, 10, and 12.5 minutes, respectively. Furthermore, to investigate the impact of the N_2/Ar gas ratio, additional AlN films were deposited with the N_2/Ar gas ratio varied from 2 : 1 to 1 : 1, 1 : 2, and 1 : 3, while keeping the sputtering power constant at 450 W and the deposition time fixed at 2.5 minutes.

AlN film surface morphology was analyzed by SEM (SU8600, 0.8 kV). Film thickness was measured by spectroscopic ellipsometry (EASEM-2000U, 70°, 400–850 nm). PXRD (Bruker D8 ADVANCE, $0.01° \text{ s}^{-1}$, 30–55° 2θ) characterized crystal structure. Electrical properties were assessed using a Keithley 4200 at room temperature. Chemical bonding was examined *via* XPS (Thermo Fisher ESCALAB Xi⁺).

Fig. 1(a) shows the diagram of the memristor device that is contracted by AlN thin film with sandwich structure. The SEM image shows that a continuous AlN film is generated, and the microstructure is mainly island particle nucleation (Fig. 1(b)). The thicknesses of AlN films were investigated by adjusting the growth times of 2.5 min, 5 min, 7.5 min, 10 min and 12.5 min at room temperature, respectively. As shown in Fig. 1(c), the thicknesses of AlN films gradually increased from ~9 nm to ~32 nm with the extension of growth time (Detailed material characterization in Fig. S1). The electrical characteristics of the prepared Al/AlN/W RRAM device are tested to perform the bias

voltage on the Al top electrode with grounding the W bottom electrode. The current compliance (I_{CC}) is subject to 1 mA to avoid a hard breakdown,[19] and the prepared memristors all required different applied voltage to accomplish the formation process. Fig. 1(d) depicts the *I–V* forming curves of AlN memristors prepared at different growth times. When the forward (positive) voltage is applied to ~4.6 V, the current of the AlN memristors prepared by growing for 2.5 min suddenly increases, which indicates the device is successfully changed from the high resistive state (HRS) to the low resistive state (LRS). With the extension of growth time, the prepared device requires a higher positive voltage to complete the formation process. This is because the increased thicknesses of AlN films calls for a larger applied voltage to form a conduction path.[20] Therefore, the thicknesses of AlN films directly impact the forming process. Considering the relatively low operating voltage for low power consumption, a growth duration of 2.5 minutes was selected to prepare the AlN memristor, and Al-rich AlN memristors were investigated with various ratios of N_2/Ar sputtering gases in detail.

Unipolar resistive switching characteristics were observed in AlN devices prepared with different N_2/Ar ratios. As shown in Fig. 2(a), the forming voltage gradually decreases from 3.2 V to 2.3 V when the N_2/Ar ratio decreases. This phenomenon may be attributed to the increased Ar ratio during sputtering, leading to non-stoichiometric composition and the formation of Al-rich AlN films,[20] which facilitates the establishment of conductive paths.[16] Fig. 2(b) shows the log *I–V* curves of Al/AlN/W devices
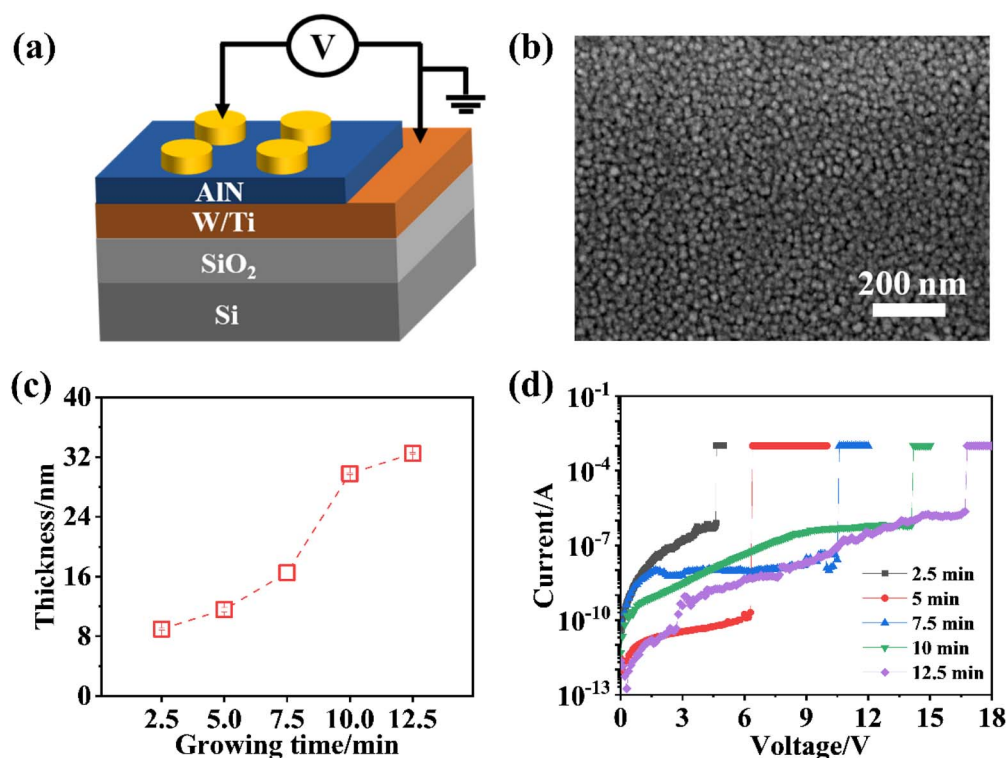

Fig. 1 (a) Schematic diagram of the Al/AlN/W device; (b) surface SEM image; (c) plot of AlN film thickness; (d) *I–V* electroforming curves of Al/AlN/W devices.
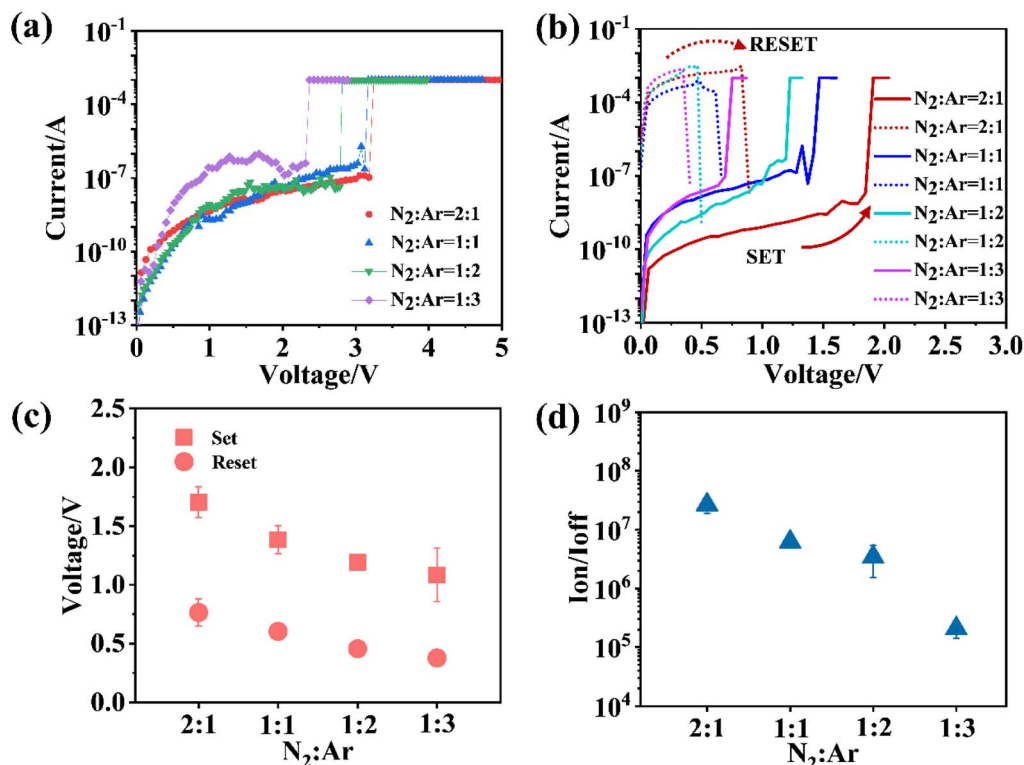
Fig. 2 (a) *I–V* electroforming curves; (b) *I–V* unipolar resistive switching curves; (c) variations in the Set voltage and Reset voltage; (d) changes in the on/off ratio with 0.1 V read voltage.

with varying N_2/Ar ratios; solid and dashed lines represent the Set and Reset processes, respectively. As shown in the solid lines, the current abruptly increases at a certain voltage, likely due to the electroformation of conductive filaments.[21,22] As shown in the dashed lines, the current sharply decreases as Joule heating under high-current conditions causes the filament to rupture at its weakest point, characteristic of unipolar resistive switching behavior.[23] The lack of switching activity during negative sweeps rules out bipolar mechanisms, reinforcing the conclusion that intrinsic Al filament formation/rupture drives the unipolar behavior (Fig. S2(a)). The relationship between the operating voltage and the N_2/Ar ratios exhibits a monotonic trend, with a gradual decrease as the N_2/Ar ratio is reduced (Fig. 2(c)). When the N_2/Ar ratio decreases from 2 : 1 to 1 : 3, there is a notable a decline in the set voltage from 1.7 V to 1.1 V, accompanied by a reduction in the Reset voltage from 0.8 V to 0.4 V. The reduction in the N_2/Ar ratio correlates with a decrease in the operating voltage could be possibly due to the increased concentration of Ar could promote the generation of Al atoms, resulting in the formation of Al-related conductive filaments.[20,24] Furthermore, the on/off ratio demonstrates a pronounced dependence on the N_2/Ar ratio, the trend observed is consistent with the aforementioned Set and Reset voltage behaviors. Similarly, Al-rich AlN films lead to the electroformation of a more conductive film, which reduces resistance and lowers the on/off ratio, making it challenging to achieve both a high on/off ratio and low operating voltage simultaneously (Fig. 2(d)).[20] To evaluate the repeatability of the

unipolar resistive switching behavior, 50 switching cycles for SET/RESET were conducted on the same device. The histogram of switching voltages over these 50 cycles is presented in Fig. S2(a). The SET voltage ranges from 0.6 to 1.4 V, with an average of 1.1 V and a standard deviation of 0.1 V. The RESET voltage ranges from 0.3 to 0.6 V, with an average of 0.4 V and a standard deviation of 0.1 V. The endurance and retention are shown in Fig. S2(b)–(d), demonstrating reproducible low-voltage operation and long-term retention time of $\sim10^3$ s.[13]

For the investigation of the aforementioned variation, the prepared AlN films were characterized by XPS and the Al 2p peaks were further analyzed to determine the types of these chemical bonds. Fig. 3(a) shows the XPS fitting results of AlN films. The subpeak of ~72.8 eV can be attributed to the Al–Al bond, and the subpeak of ~73.5 eV is the Al–N bond.[25] As illustrated in Fig. 3(b), the XPS analysis reveals a gradual increase in the Al–Al bond content as the N_2/Ar ratio decreases. When the N_2/Ar ratio is reduced from 2 : 1 to 1 : 3, there is a marked rise in the Al–Al bond content, indicating a significant Al-rich AlN films and enhancement in the formation of these bonds in AlN films.[16,26] This trend confirms that the films prepared under conditions favoring higher Ar ratios are enriched with Al, featuring free Al atoms and potentially nanoparticles formed through agglomeration during the sputtering process. While trace Al–O bonding (74.5 eV) is detected, its intensity is <10% of Al–Al peaks, indicating oxygen incorporation is negligible for conduction.[25] Al-rich AlN films were obtained by N_2/Ar ratio adjustment, where these Al elements
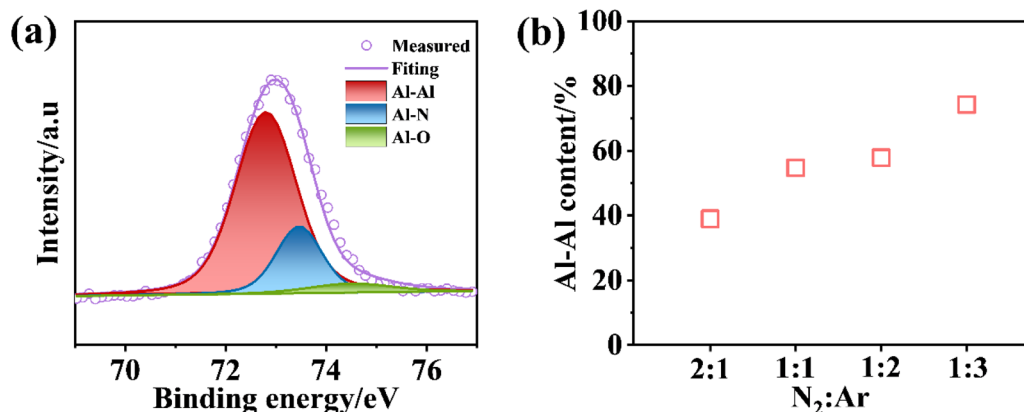
Fig. 3 (a) XPS spectra of the AlN film prepared under N_2/Ar ratio of 1 : 3; (b) variation in the Al−Al bond content as determined by fitting the XPS results.

play a crucial role in facilitating the electroformation of conductive filaments during the Set process. Moreover, this stoichiometry tuning engineering, achieved by adjusting the N_2/Ar ratio, provides an effective approach for realizing low operating voltages.

Furthermore, logarithmic plots depicting the relationship between voltage (V) and current (I) were generated to examine the conduction mechanisms, as presented in Fig. 4(a). For the HRS of unipolar devices, in the low-voltage regime, the I–V characteristics of the device approximately follow Ohm's law ($I \propto V^1$).[27] As the applied bias increases, an increase in the slope of the Log I–Log V curve to approximately 2.2 ($I \propto V^2$), consistent with Child's law. With further increase in bias, the current exhibits a steep rise ($I \propto V^n$, where $n > 2$). The I–V characteristics
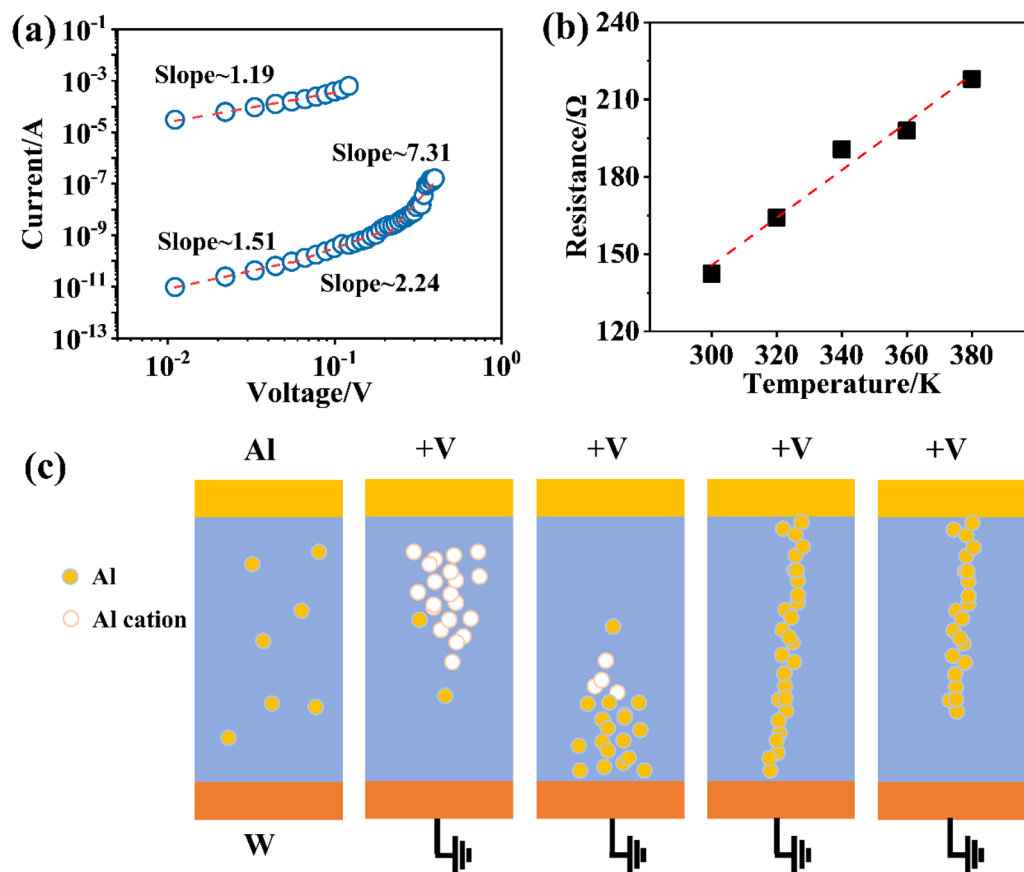

Fig. 4 (a) Logarithmic plots of current (I) versus voltage (V) for the SET and RESET processes and (b) variation of LRS resistance with different temperature prepared at N_2/Ar ratios of 1 : 3, (c) schematic illustration of the formation and rupture of conductive filaments in the Al/AlN/W device.

Table 1 Comparison of performance parameters of our unipolar memristor with those of the reported unipolar memristors

Memristor structure	Bandgap (eV)	Set voltage (V)	Reset voltage (V)	On/off ratios	References
p^+-Si/n-ZnO/Al	3.37	7	3	$\sim 10^3$	31
Pt/ZnO : Al/ZnO/Pt	3.37	±1.5	±0.5	215	32
Au/FeZnO/MgO/Pt	3.37	3.5	1.2	$\sim 10^5$	33
Ta/Ta$_2$O$_5$/Pt	4.2	1.53	0.87	50	34
Au/TaO$_x$/SnO$_2$	4.2	−0.8	−1.5	200	11
Pt/Ga$_2$O$_3$/Pt	4.9	3.2	0.99	5×10^7	35
Ag/Ga$_2$O$_3$/Pt	4.9	$\sim$3.5 V	0.67	$\sim 10^6$	10
Ag/HfO$_x$/Pt	5.5	1.05–1.2	0.2–0.5	$\sim 10^3$	36
Pt/AlN : Cu/Pt	6.2	±2	±0.7	$\sim 10^2$	37
Pt/Al/AlN/Pt	6.2	1.25	0.25	$\sim 10^3$	38
Al/AlN/Al	6.2	$\sim$2.5	$\sim$1.5	$\sim 10^5$	39
Al/AlN/W	6.2	$\sim$1.1	$\sim$0.4	$\sim 10^5$	This work

are predominantly governed by the space-charge-limited current (SCLC) mechanism.[10,28] For the LRS of unipolar devices, the slope of the Log I–Log V curve ranges from 0.93 to 1.19 ($I \propto V$), which is consistent with Ohm's law. This verifies that the LRS is primarily characterized by the electroformation of conductive filaments. To investigate the composition of conductive filaments in the LRS, a variable temperature test was performed on the I–V characteristics of the Al/AlN/W device, as illustrated in Fig. 4(b). The resistance was found to increase with temperature from 300 K to 380 K, exhibiting behavior consistent with typical metallic conductivity, which reconfirms the electroformation of metallic conductive filaments under the LRS conditions.[29] Data collected over this temperature range were subjected to linear fitting, yielding the formula $R(T) = R_0[1 + \alpha(T - T_0)]$, where R_0 (142.3 Ω) represents the resistance at the reference temperature T_0 (300 K); both are constants. Analysis of the fitted curve (depicted by the red line) enabled the determination of $\alpha = 6.5 \times 10^{-3}$ K^{-1}, a value consistent with the temperature coefficient of Al conductive wires.[30] This observation further corroborates the conclusion that the conductive filaments formed are indeed composed of Al aligning with the aforementioned findings.

Based on the aforementioned analysis and discussion, we propose a potential operating mechanism to elucidate the resistive switching behavior of the device, as illustrated in Fig. 4(c). In Al-rich AlN thin films, there exist electrochemically active Al metal atoms. Upon the application of an electric field, the oxidation of Al can generate additional Al ions, which migrate toward the cathode under the influence of the field. Simultaneously, these discontinuous Al atoms collaborate to form Al-related conductive filaments, thereby facilitating the transition of the device back to the LRS. During the SET process, a compliance current is applied to control the conductive filament size and prevent device damage. In contrast, during RESET, the compliance current is removed, allowing higher current flow through the Al-based conductive paths. This leads to significant localized Joule heating, which raises the temperature within the filaments, inducing Al atom diffusion and filament rupture. Consequently, the device switches from the LRS to the HRS, exhibiting unipolar resistive switching

behavior. The formation and disruption of Al-based conductive filaments are considered the most plausible switching mechanism underlying the device's operation.

Therefore, the approach of stoichiometry tuning engineering, by altering the N$_2$/Ar ratios, this method proves to be an efficient strategy for regulating the operating voltage and achieving low-voltage unipolar memristors with a high switching on/off ratio. Table 1 provides a comparative analysis of the performance parameters of our unipolar memristor alongside other memristors reported in the literature, specifically focusing on the switching voltage and current on/off ratios. The fabricated memristor demonstrates a lower operating voltage and a higher on/off ratio with the widest bandgap compared to previously reported devices. This work establishes Al tuning engineering as an effective approach for low-voltage unipolar operation in AlN memristors, achieving superior on/off ratios (>10^5) at $\sim$1 V operation. Though reliability requires further improvement, the fundamental insights into filament control *via* sputtering modulation provide a viable path forward.

In summary, we have successfully fabricated unipolar Al/AlN/W memristors using a straightforward magnetron sputtering techniques. Our study reveals that the impact of Al stoichiometry on both the fabrication and electrical characteristics of the Al/AlN/W devices with tunable unipolar resistive switching behavior. Through an in-depth analysis of the electrical performance, XPS characterizations, and a variable temperature tests, we have elucidated the reasons for variations in unipolar resistive switching based on Al-rich films and the electroformation process of conductive filaments. This work lays a solid foundation for further research into nitride-based unipolar memristors *via* a simple method of stoichiometry tuning engineering, and the fabricated unipolar devices with low voltage and high on/off ratio hold promise for application in future high-density multi-level memory arrays.

Author contributions

Ankang Xiao: data curation (lead); investigation (lead); writing-original draft (lead); writing-review & editing (lead). Luyu Zhao: data curation (supporting); investigation (supporting). Ying

Yang: data curation (supporting); validation (supporting). Cai Jin: data curation (supporting); validation (supporting). Xiaoqin Yang: data curation (supporting). Lili Ma: data curation (supporting). Feifei Tian: investigation (supporting). Hu Wei: validation (supporting). Zengli Huang: validation (supporting). Hong Gu: data curation (supporting); investigation (supporting); writing-original draft (supporting); writing-review & editing (supporting); resources.

Conflicts of interest

The authors declare that they have no known competing financial interests that could have appeared to influence the work reported in this paper.

Data availability

The data that support the findings of this study are available within the article and its supplementary information (SI). Supplementary information is available. See DOI: https://doi.org/10.1039/d5ra05691h.

Acknowledgements

References

1 M. S. B. Hoque, Y. R. Koh, J. L. Braun, A. Mamun, Z. Liu, K. Huynh, M. E. Liao, K. Hussain, Z. Cheng, E. R. Hoglund, D. H. Olson, J. A. Tomko, K. Aryana, R. Galib, J. T. Gaskins, M. M. M. Elahi, Z. C. Leseman, J. M. Howe, T. Luo, S. Graham, M. S. Goorsky, A. Khan and P. E. Hopkins, *ACS Nano*, 2021, **15**, 9588–9599.

2 P.-H. Hung, C.-Y. Li, K.-P. Min, C.-C. Lin and S.-Y. Chu, *AIP Adv.*, 2020, **10**, 045017.

3 Y. Yang, H. Li and Q. Hua, *Mater. Futures*, 2025, **4**, 032701.

4 C. Chen, Y. C. Yang, F. Zeng and F. Pan, *Appl. Phys. Lett.*, 2010, **97**, 083502.

5 X. Shen, H. Gao, Y. Duan, Y. Sun, J. Guo, Z. Yu, S. Wu, X. Ma and Y. Yang, *Appl. Phys. Lett.*, 2021, **118**, 183503.

6 K.-P. Min, C.-Y. Li, T.-J. Chang and S.-Y. Chu, *ACS Appl. Electron. Mater.*, 2021, **3**, 5327–5334.

7 W. Ahn, S. Lee, J. Oh, H. Lee and S. Y. Choi, *Adv. Mater.*, 2024, **37**, 2413640.

8 X. Dai, Q. Hua, C. Jiang, Y. Long, Z. Dong, Y. Shi, T. Huang, H. Li, H. Meng, Y. Yang, R. Wei, G. Shen and W. Hu, *Nano Energy*, 2024, **124**, 109473.

9 B. J. Choi, A. C. Torrezan, J. P. Strachan, P. G. Kotula, A. J. Lohn, M. J. Marinella, Z. Li, R. S. Williams and J. J. Yang, *Adv. Funct. Mater.*, 2016, **26**, 5290–5296.

10 D. Cui, Y. Du, Z. Lin, M. Kang, Y. Wang, J. Su, J. Zhang, Y. Hao and J. Chang, *IEEE Electron Device Lett.*, 2023, **44**, 237–240.

11 C. Du, X. Ji, Z. Dong, D. Gu, B. Yan, X. Hu, Y. Zhou, J. Yan, L. Wang, S. Duan and G. Zhou, *J. Alloys Compd.*, 2025, **1010**, 177020.

12 S. Wang, B. Dang, J. Sun, M. Zhao, M. Yang, X. Ma, H. Wang and Y. Hao, *IEEE Electron Device Lett.*, 2021, **42**, 700–703.

13 K. Zhang, X. Zhao, Y. Han, K. Hu, Y. Zhang, L. Li, Q. Zhou, X. Shan, X. Lin, K. Shan, Z. Ma, Q. Liu, Z. Song and F. Wang, *Adv. Electron. Mater.*, 2022, **8**, 2200702.

14 Y. Zhang, G. Tang, P. Feng, K. Kang, X. Tang, M. Li and W. Hu, *Appl. Phys. Lett.*, 2022, **121**, 163502.

15 M. Jiang, B. Wang, K.-H. Xue, N. Liu, H. Sun, H. Lu and X. Miao, *Appl. Phys. Express*, 2019, **12**, 104003.

16 Y. Liu, T. P. Chen, P. Zhao, S. Zhang, S. Fung and Y. Q. Fu, *Appl. Phys. Lett.*, 2005, **87**, 033112.

17 K. Sato, J. Ohta, S. Inoue, A. Kobayashi and H. Fujioka, *Appl. Phys. Express*, 2009, **2**, 011003.

18 Y. Song, F. Kawamura, K. Shimamura, T. Ohgaki and N. Ohashi, *AIP Adv.*, 2020, **10**, 115011.

19 Y. Wang, X. Liu, Y. Chen, W. Xu, D. Liang, F. Gao, M. Zhang, S. Samanta, X. Gong, X. Lian, X. Wan and Y. Tong, *Appl. Phys. Express*, 2019, **12**, 106504.

20 Z.-L. Tseng, L.-C. Chen, W.-Y. Li and S.-Y. Chu, *Ceram. Int.*, 2016, **42**, 9496–9503.

21 Y. Fu, C.-C. Huang and J.-C. Wang, *Microelectron. Eng.*, 2019, **216**, 111033.

22 K. Liu, F. Wang, X. Shan, K. Shan, Z. Ma, K. Hu, H. Guo, Z. Song and K. Zhang, *Appl. Phys. Express*, 2023, **16**, 061007.

23 H. Sharma, N. Saini, Lalita, D. Kaushik, A. Kumar and R. Srivastava, *RSC Adv.*, 2024, **14**, 14910–14918.

24 W. Zhu, T.-T. Guo, L. Liu and R.-R. Zhou, *Acta Phys. Sin.*, 2021, **70**, 068502.

25 L. Rosenberger, R. Baird, E. McCullen, G. Auner and G. Shreve, *Surf. Interface Anal.*, 2008, **40**, 1254–1261.

26 W. Zhu, T. P. Chen, Z. Liu, M. Yang, Y. Liu and S. Fung, *J. Appl. Phys.*, 2009, **106**, 093706.

27 C. Yao, J. Li, H. Zhang and T. Tian, *ACS Omega*, 2024, **9**, 33941–33948.

28 T.-M. Liu, Z.-W. Wu, C.-C. Lee, P.-Q. Yang, H.-S. Hsu and F.-Y. Lo, *AIP Adv.*, 2024, **14**, 115023.

29 D. Xu, Y. Xiong, M. Tang and B. Zeng, *J. Alloys Compd.*, 2014, **584**, 269–272.

30 A. I. Oliva and J. M. Lugo, *Int. J. Thermophys.*, 2016, **37**, 35.

31 L. Zhang, L. Zhu, X. Li, Z. Xu, W. Wang and X. Bai, *Sci. Rep.*, 2017, **7**, 45143.

32 Z.-J. Liu, J.-Y. Gan and T.-R. Yew, *Appl. Phys. Lett.*, 2012, **100**, 153503.

33 Y. Zhang, Z. Duan, R. Li, C.-J. Ku, P. I. Reyes, A. Ashrafi, J. Zhong and Y. Lu, *J. Phys. D: Appl. Phys.*, 2013, **46**, 145101.

34 S. Gao, G. Liu, Q. Chen, W. Xue, H. Yang, J. Shang, B. Chen, F. Zeng, C. Song, F. Pan and R.-W. Li, *ACS Appl. Mater. Interfaces*, 2018, **10**, 6453–6462.

35 D. Cui, M. Pei, Z. Lin, Y. Wang, H. Zhang, X. Gao, H. Yuan, Y. Li, J. Zhang, Y. Hao and J. Chang, *Chip*, 2025, **4**, 100122.

36 Y. Wang, G. Zhou, B. Sun, W. Wang, J. Li, S. Duan and Q. Song, *J. Phys. Chem. Lett.*, 2022, **13**, 8019–8025.

37 C. Chen, S. Gao, G. Tang, C. Song, F. Zeng and F. Pan, *EEE Electron Device Lett.*, 2012, **33**, 1711–1713.

38 J. Wen, W. Hua, Q. K. Gong and B. Wang, *J. Ovonic Res.*, 2022, **18**, 815–825.

39 H. Qin, N. He, C. Han, Y. Wang, R. Hu, J. Wu, W. Shao, H. Fang, H. Zhang, X. Wang, Y. Liu and Y. Tong, *Appl. Phys. Lett.*, 2025, **127**, 023501.